



OPEN

Controlling viscous fingering instabilities of complex fluids

Alban Pouplard & Peichun Amy Tsai✉

Despite their aesthetic elegance, wavy or fingering patterns emerge when a fluid of low viscosity pushes another immiscible fluid of high viscosity in a porous medium, producing an incomplete sweep and hampering several crucial technologies. Some examples include chromatography, printing, coating flows, oil-well cementing, as well as large-scale technologies of groundwater and enhanced oil recovery. Controlling such fingering instabilities is notoriously challenging and unresolved for complex fluids of varying viscosity because the fluids' mobility contrast is often predetermined and yet the predominant drive in determining a stable, flat or unstable, wavy interface. Here we show, experimentally and theoretically, how to suppress or control the primary viscous fingering patterns of a common type of complex fluids (of shear-thinning with a low yield stress) using a radially tapered cell of linearly varying gap thickness, $h(r)$. Experimentally, we displace a complex viscous (PAA) solution with gas under a constant flow rate (Q), varied between 0.02 and 2 slpm (standard liter per minute), in a radially converging cell with a constant gap-thickness gradient, $\alpha = dh/dr < 0$. A stable, uniform interface emerges at low Q and in a steeper cell (i.e., greater $|\alpha|$) for the complex fluids, whereas unstable fingering pattern at high Q and smaller $|\alpha|$. Our theoretical predictions with a simplified linear stability analysis show an agreeable stability criterion with experimental data, quantitatively offering strategies to control complex fluid-fluid patterns and displacements in microfluidics and porous media.

The process of one fluid pushing another is ubiquitous while involving fascinating and complex patterns stemming from flow instabilities. During immiscible displacement of more-viscous fluid pushed by another less-viscous one in a porous media, the mobility contrast results in the tunneling of the displacing fluid and hence fingering patterns, hindering a full swipe of the displaced fluid. As the utmost detrimental, limiting factor in enhanced oil recovery processes, this so-called viscous fingering or Saffman–Taylor instability^{1–5} has been extensively studied since the 1980s. In particular, a convenient paradigm of Hele–Shaw cells consisting of two parallel plates spaced with a constant gap thickness yielding a homogeneous permeability is often used to understand the effects of inertia, gravity, and rotation. Recent studies using simple fluids of constant viscosity have considered centrifugally driven viscous fingering via rotation⁶ and found that the inertia tends to increase the finger-width⁷ and curvature-dependent surface tension can theoretically lead to the stabilization (destabilization) of conventionally unstable (stable) situations⁸. In the last two decades, studies of viscous fingering have been extended to complex fluids, usually leading to wider fingers compared to the simple Newtonian counterparts⁹. Intriguing side-branching patterns with multiple small sided-fingers are often observed with complex, yield-stress fluids¹⁰ in a uniform cell.

The control of the fingering instabilities plays a significant role in enhancing the efficiency of various technological applications, e.g., chromatography separation¹¹, printing devices¹², coating¹³, oil-well cementing, and large-scale enhanced oil recovery¹⁴. For simple Newtonian fluids, several strategies have recently been developed to suppress the fingering instability, for example, using time-dependant injection flow rate^{15–17}, an elastic confinement^{18–20}, a gap-gradient cell^{21–23}, and an external electric field²⁴. Nevertheless, such crucial control of the primary viscous fingering instability has not been reported for complex fluids, which are commonly present in natural and industrial settings. Here, we demonstrate the feasibility of inhibiting the viscous fingering instability of complex fluids of shear-thinning with a low-yield stress using a radially-tapered narrow cell using experiment and theory.

Experimentally, we prepare two different aqueous solutions (S_a and S_b) of PolyAcrylic Acid (PAA) to have different viscosity contrasts as the complex displaced fluid (see “Methods”). We first fill in one complex PAA solution in a radial cell and subsequently inject a gas (nitrogen, viscosity $\mu_1 = 1.76 \times 10^{-5}$ Pa · s at 20 °C) as a pushing fluid 1 (see Fig. 1a,b). The gas is injected at a constant flow rate, Q , ranging from 0.02 to 2 slpm (standard

Department of Mechanical Engineering, University of Alberta, Edmonton, AB T6G 2G8, Canada. ✉email: peichun.amy.tsai@ualberta.ca

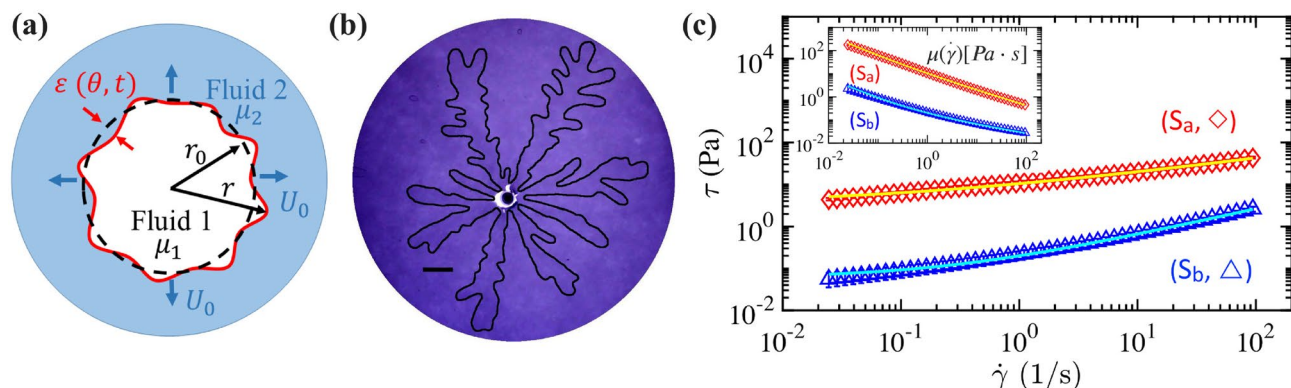


Figure 1. (a) Top-view schematics of the fluid–fluid displacement experiment where one less viscous complex fluid 1 of varying viscosity (μ_1) with shear rate ($\dot{\gamma}$) is pushing another immiscible one, denoted as complex fluid 2 with changing viscosity (μ_2). (b) Representative experimental snapshot of complex viscous fingering produced with a complex yield-stress (PAA) solution (S_a) displaced by a gas injected with a flow rate $Q = 0.2$ slpm (standard liter per minute) in a flat Hele–Shaw cell, under the mobility contrast $\mathcal{M}_c = \mu_2/\mu_1 = 5.58 \times 10^4$ and at the interface velocity $U_0 = 14.3$ mm/s. The scale bar corresponds to 2 cm. (c) Flow curves of shear stress, τ , and viscosity, μ , depending on shear rate ($\dot{\gamma}$) for the two complex solutions used: (S_a , \diamond) and (S_b , \triangle). The lines in (c) correspond to the best fits of the data to the Herschel–Bulkley model (Eq. 1).

liter per minute) by a flow controller (Alicat) with an accuracy of 1 ml/min. Figure 1c shows the rheological measurements (Anton Paar MCR302) of the shear stress (τ) varying with shear rate ($\dot{\gamma}$) for the two complex solutions; (S_a) is more viscous than (S_b). Neglecting the elastic properties (see “Methods” for the justification), the flow curve data shows an excellent fit with the common Herschel–Bulkley (HB) model²⁵:

$$\tau = \tau_c + \kappa \dot{\gamma}^n, \quad (1)$$

where τ_c , κ , and n correspond to the yield stress, consistency index, and power-law index, respectively.

The viscosity data (μ) varying with shear rate ($\dot{\gamma}$) is well described by the corresponding HB model (Eq. 1) via $\mu \equiv \tau/\dot{\gamma} = \tau_c/\dot{\gamma} + \kappa \dot{\gamma}^{n-1}$, shown in Fig. 1c inset. Table 1 summarizes the best nonlinear-fit results of the rheological measurements of $\tau = f(\dot{\gamma})$ for $0.025 \leq \dot{\gamma} \leq 86 \text{ s}^{-1}$. The corresponding HB fitting functions are plotted as lines in Fig. 1c. Both solutions are shear-thinning, with decreasing viscosity with increasing $\dot{\gamma}$, i.e., $n < 1$. However, the neutralized PAA solution with NaOH (S_a) is more viscous, by $\approx 15 \times -70 \times$ than (S_b) without NaOH depending on $\dot{\gamma}$, and has a greater τ_c but a smaller n .

Results and discussion

Using flat Hele–Shaw cells of a fixed gap thickness, we observe complex fingering patterns, which overall resemble the classical viscous fingering for simple Newtonian fluids but has complex side-fingers along the side of the major fingers, as shown in Fig. 1b. In agreement, similar patterns were observed previously, referred as side-branching²⁶ or the elasto-inertial regime^{27,28} in a uniform cell. Interestingly, the side-branched fingers can be obtained only at high flow rates ($Q \geq 1.5$ slpm) for the less viscous fluid (S_b) but for all the experimental range of $Q = 0.02 - 1.5$ slpm for the more-viscous fluid (S_a).

When using a radially converging cell of a constant and negative gap-thickness gradient, $\alpha = dh(r)/dr$ (see Fig. 2a), we stopped observing side-branched fingers but smooth classical viscous fingers for more-viscous (S_a) with using $Q = 0.02 - 1.5$ slpm. This is consistent with a recent experimental study²⁹, revealing mitigation of side-branching, but not inhibition of the primary viscous fingering, for a complex yield-stress fluid in a rectangular tapered cell. Is it even possible to eliminate complex viscous fingerings for an unfavorable mobility contrast, $\mathcal{M}_c \sim \mu_2/\mu_1 > 1$? To answer this critical question, we systematically conduct experiments of a gas pushing a PAA complex fluid under various flow rates (Q) and five different taper gradients (α). Using a different complex solution, remarkably, with suitable rheological and flow parameters, we can control and inhibit the primary fingering instability and observe complete stable and flat interfaces between the pushing Newtonian gas and the displaced, complex fluid (S_b) (of $\mathcal{M}_c \approx 10^3 - 10^5$), as illustrated by a fully circular displacement front, i.e., stable interface, in Fig. 2c.

Figure 2d shows the experimental phase diagram of unstable versus stable displacements manifested in wavy fingering (e.g., Fig. 2b) or a smooth circular (e.g., Fig. 2c) interfacial pattern, when the gas is pushing the complex

Complex solution	PAA (wt %)	NaOH (wt %)	τ_c (Pa)	κ (Pa·s ⁿ)	n
(S_a)	0.10	0.034	3.29	7.12	0.37
(S_b)	0.10	0	0.06	0.14	0.63

Table 1. Rheological parameters for the two complex fluids with the HB model (Eq. 1).

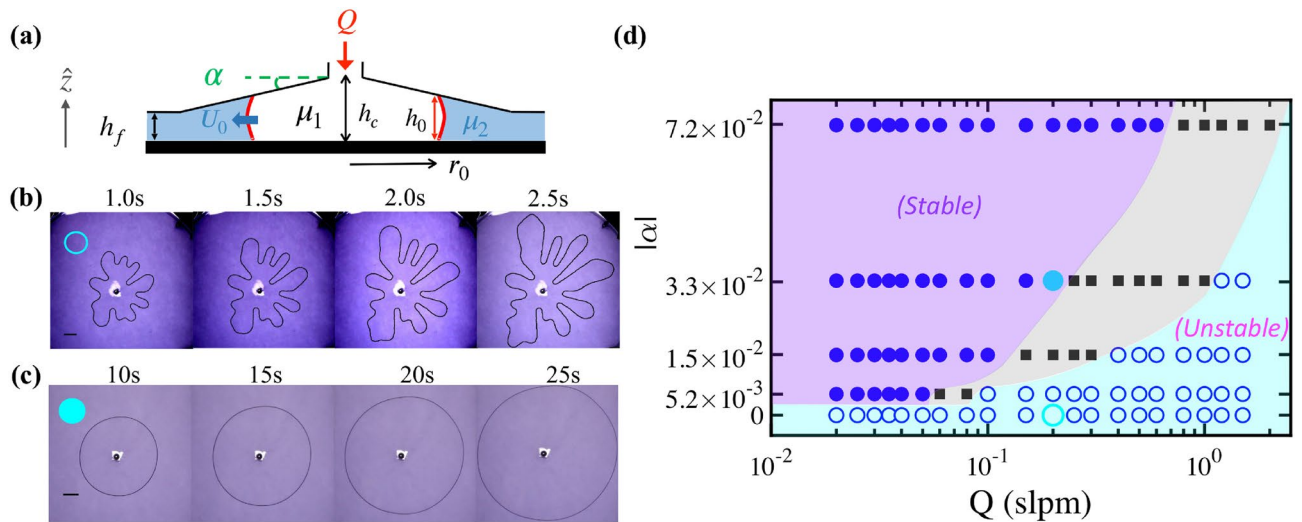


Figure 2. Control of complex viscous fingering using a radially-tapered cell, with a linearly varying gap thickness ($h(r) = h_c + \alpha r$), schematically shown in (a), the side-view of the experiment. Here, h_c is the gap-thickness at the cell centre ($r = 0$). (b) Experimental snapshots of a branched viscous fingering pattern observed when a gas is pushing the complex solution (S_b) in a flat Hele-Shaw cell with $h_c = 0.5$ mm and $Q = 0.2$ slpm (standard liter per minute). (c) By contrast, snapshots of a stable interface obtained when the gas is pushing (S_b) in a tapered cell of the gap gradient $\alpha = -3.33 \times 10^{-2}$, with $h_c = 5.16$ mm and $Q = 0.2$ slpm. The scale bars in (b) and (c) represent 20 mm. (d) Experimental results of stability diagram, with uniform stable (filled circle) versus fingering/wavy unstable interfaces (open circle) under various values of flow rate, Q , and the tapered gap gradient, $|\alpha|$. Black squares (■) represent a transitional state where the interface starts to develop a wavy profile.

fluid (S_b) under various values of α and Q . We differentiate three types of displacements observed during the experiments with the fluid (S_b), namely uniform stable (filled circle, ●), fingering/wavy unstable (open circle, ○), and transitional (filled square, ■) displacements. The latter corresponds to the transitional state where the interface starts to develop a wavy profile.

A crucial observation from Fig. 2d is that, firstly, a stable interface accompanying with a full displacement occurs at low Q in a converging-gap cell, whereas an unstable interface with fingering pattern always happen in a uniform-gap cell (of $\alpha = 0$). Secondly, a steeper converging gap gradient helps stabilize the interface, and the transition from stable to unstable interfaces happens at a higher flow rate Q as the gap-gradient value $|\alpha|$ is increased. Thirdly, such experimental stability diagram is established only for the complex fluid (S_b) since a complete sweep has never been observed with our experimental parameters for the more-viscous fluid (S_a) of a high mobility contrast, $\mathcal{M}_c = \mu_2/\mu_1 = 2.68 \times 10^4 - 1.16 \times 10^7$. The complex fluid (S_b) has a lower and small \mathcal{M}_c -range of $1.61 \times 10^3 - 1.67 \times 10^5$ than (S_a). These contrast results between the two complex solutions highlight not only the complexity but also the importance of rheological parameters, via κ , n and local $\dot{\gamma}$, in controlling complex viscous fingering.

To gain physical insights, we develop a simplified linear stability analysis generalized to two yield-stress, power-law fluids (Fluid 1 pushing Fluid 2) in a radially-tapered cell, as depicted in Fig. 2a. The introduction of a constant gap gradient (α) produces a linearly-varying height, $h(r)$, between the two plates of the cell so that $h(r) = h_c + \alpha r$, where h_c is the gap-thickness at the cell centre ($r = 0$). Considering the fluids' interface at $r = r_0$, the height can be expressed as $h(r) = h_0 + \alpha(r - r_0)$, with h_0 the gap-thickness at the fluid-fluid interface. For fluids in the narrow gap, we use a modified Darcy's law replacing the constant viscosity (μ), typically applicable for a simple Newtonian fluid, by the effective shear-dependent viscosity, μ_{eff} , to approximate the complex fluid's velocity in a homogeneous porous medium. Although this model may not be rigorously accurate for all types of non-Newtonian fluids in different flow regimes^{30,31}, the applicability of this approximation has been verified numerically for a Bingham fluid at low-pressure, one-channel and high-pressure, fully flowing regimes³¹ and validated experimentally for weakly shear-thinning fluids³² and for yield-stress gel solution (of shear-thinning [$n \approx 0.4$] and with a yield stress ranging from 10 to 50 Pa)²⁶. Since our complex fluids, S_a and S_b , are shear-thinning with less important values of yield-stress, the applicability of the modified Darcy's law describing our complex fluids' velocity field may be expected and allows us to arrive at an analytical solution (given below).

Neglecting the fluids' elastic properties (justified in the Section of "Methods"), the governing equations of the immiscible, complex fluids are the continuity equation (taking gap-variation into account) and 2D depth-average modified Darcy's law using μ_{eff} :

$$\nabla \cdot (h\mathbf{U}_j) = 0 \quad \text{and} \quad \mathbf{U}_j = -\frac{h^2}{12\mu_{\text{eff}}} \bar{\nabla} P_j, \quad (2)$$

where $U_j(r, \theta) = (u_{rj}, u_{\theta j})$ and $P_j(r, \theta)$ are the depth-average velocity and pressure fields of the fluid indexed j , respectively. j represents the two complex fluids during the fluid-fluid displacement process; $j = 1$ (2) denotes the pushing (displaced) fluid.

The complex fluid's viscosity ($\mu_{\text{eff}j}$) is modeled using the Herschel–Bulkley law (see Eq. 1) for yield-stress fluids, with the local shear rate approximated by $\dot{\gamma}(r) = u_{rj}/h(r)$, and can be expressed as: $\mu_{\text{eff}j} = \frac{\tau_{cj}}{\dot{\gamma}} + \kappa_j \dot{\gamma}^{n_j-1}$, with yield stress (τ_{cj}), consistency index (κ_j), and power-law index (n_j). The depth-average continuity equation can be expressed using the pressure field (P_j) and further simplified. By setting $n_j = 1$ and $\tau_{cj} = 0$, we obtain and recover the simple Newtonian fluid case: $\frac{\partial^2 P_j}{\partial r^2} + \frac{1}{r} \frac{\partial P_j}{\partial r} + \frac{3\alpha}{h} \frac{\partial P_j}{\partial r} + \frac{1}{r^2} \frac{\partial^2 P_j}{\partial \theta^2} = 0^{22}$.

In the linear stability analysis, the pressure field is expressed as the solutions of the base state and the perturbation, $\epsilon(\theta, t) = \epsilon_0 r_0(t) \exp(ik\theta + \sigma t)$:

$$P_j(r, \theta, t) = f_j(r) + g_{kj}(r)\epsilon(\theta, t), \tag{3}$$

where $f_j(r)$ corresponds to the base-state pressure when the interface is stable and independent of θ . The term of $g_{kj}(r)\epsilon$ represents the perturbation that propagates along the interface with wavenumber, k , and the growth rate of the perturbation, σ . We employ the kinematic boundary conditions, i.e., two complex fluids moving at the same velocity at the interface, and the Young–Laplace equation for the pressure jump at the interface due to surface tension and curvature. To obtain analytical solutions, we assume that the fluid yield stress is negligible compared to the viscous stress, i.e., small Bingham ($Bn_j \ll 1$) situation, where the Bingham number is the ratio of the yield to viscous stress: $Bn_j = \frac{\tau_{cj}}{\kappa_j \left(\frac{u_{rj}}{h}\right)^{n_j}}$. Focusing on the moment when the perturbation starts to propagate, implying small perturbation ($\epsilon \ll 1$), $\epsilon_0 \ll 1$, $g'_{kj}(r)\epsilon \ll f'_j(r)$, and negligible high-order terms of $O(\epsilon^2)$, we obtain the dimensionless dispersion relation Eq. (4) below, with the dimensionless growth rate, $\bar{\sigma} = \frac{\sigma r_0}{U_0}$, and the dimensionless wavenumber, $\bar{k} = k$ (see Supplementary Information for the detailed derivation):

$$\begin{aligned} \frac{12\bar{\sigma}h_0}{\gamma} \left(\kappa_1 \sqrt{n_1} \left(\frac{U_0}{h_0}\right)^{n_1} + \kappa_2 \sqrt{n_2} \left(\frac{U_0}{h_0}\right)^{n_2} \right) &= -\frac{12U_0}{\gamma} (\sqrt{n_1}\mu_1|_{r=r_0} + \sqrt{n_2}\mu_2|_{r=r_0}) \\ &- \frac{12\alpha r_0}{\gamma} (2\sqrt{n_1}\tau_{c1} + 2\sqrt{n_2}\tau_{c2}) \\ &- \frac{12\alpha r_0}{\gamma} \left(\kappa_1 \sqrt{n_1} \left(\frac{U_0}{h_0}\right)^{n_1} + \kappa_2 \sqrt{n_2} \left(\frac{U_0}{h_0}\right)^{n_2} \right) \\ &+ \bar{k} \left(\frac{12U_0}{\gamma} (\mu_2|_{r=r_0} - \mu_1|_{r=r_0}) + 2\alpha \cos \theta_c + \frac{h_0^2}{r_0^2} \right) - \frac{h_0^2}{r_0^2} \bar{k}^3, \end{aligned} \tag{4}$$

where γ is the interfacial tension, the complex fluids' viscosity at the interface is given as $\mu_j|_{r=r_0} = \left(\tau_{cj} + \kappa_j \left(\frac{U_0}{h_0}\right)^{n_j} \right) \frac{h_0}{U_0}$, and θ_c corresponds to the contact angle at the interface and is measured between the plate and the curved meniscus (across the gap). $\theta_c = 0$ corresponds to a completely wetting displaced fluid, whereas $\theta_c = \pi$ to a perfectly non-wetting one.

Consequently, taking $\tau_{cj} = 0$, $n_j = 1$, $\kappa_j = \mu_j$ in Eq. (4) for simple fluids, and defining the viscosity contrast $\lambda = \frac{\mu_1}{\mu_2}$ and Capillary number $Ca = \frac{12U_0\mu_2}{\gamma}$, the dispersion relation recovers to the same formula by Al-Housseiny and Stone for Newtonian fluids with constant viscosity (Eq. 24 in Ref.²²). In addition to the crucial influences of α , λ , Ca , and wetting angle (θ_c) for the simple fluid case, the derived dimensionless perturbation growth rate ($\bar{\sigma}$) as a function of (\bar{k}) depends on the fluids' rheological properties (κ_j , n_j , τ_{cj}) and the local velocity, radius, and gap thickness at the interface (U_0 , r_0 , h_0 , respectively) for the complex yield-stress fluids. The primary stabilizing mechanism for both Newtonian^{20,21,23} and Non-Newtonian viscous fingering instabilities using a converging taper is similar. That is through a stabilizing Capillary effect, via the term of $2\alpha \cos \theta_c$ in Eq. (4) as $\alpha < 0$, since the Laplace pressure becomes more significant when the fluid-fluid interface travels across a narrower gap and can overcome the destabilizing effect of the pressure gradient due to viscosity difference, via the term $\frac{12U_0}{\gamma} (\mu_2|_{r=r_0} - \mu_1|_{r=r_0})$. However, comparing the expression of the dimensionless dispersion relation (Eq. 4) to the Newtonian counterpart (in Ref.²²), we notice an additional, distinct term via $-\frac{12\alpha r_0}{\gamma} (\sqrt{n_1}\tau_{c1} + \sqrt{n_2}\tau_{c2})$, which has a positive value for a converging taper since $\alpha < 0$, while r_0 , γ , n_j , and τ_{cj} have positive values. This positive term, depending on the yield stress of the fluids, tends to increase the growth rate and, hence, has a destabilizing effect promoting the fingering instability growth, which could explain the more likely appearance of viscous fingering using complex fluids. Additionally, instead of being constant in the Newtonian case, the viscosity value depends on various factors, such as the interfacial location, thickness, and velocity as well as the rheological valuables of τ_c , k , and n . On the one hand, if the perturbation's growth rate σ is less than zero for every wavenumber, k , the interface will always be stable theoretically. On the other hand, the wavenumber at the maximum growth (\bar{k}_{max}) can be found by taking the derivative of the above dimensionless dispersion Eq. (4) with respect to \bar{k} and setting $\frac{\partial \bar{\sigma}}{\partial \bar{k}} = 0$:

$$\bar{k}_{max} = \left(\frac{\frac{h_0^2}{r_0^2} + 2\alpha \cos \theta_c + \frac{12U_0}{\gamma} (\mu_2|_{r=r_0} - \mu_1|_{r=r_0})}{3\frac{h_0^2}{r_0^2}} \right)^{\frac{1}{2}}. \quad (5)$$

\bar{k}_{max} is the wave number at the maximum growth, i.e., theoretically, the most unstable mode's wave number. Hence, $\sigma(\bar{k}_{max}) < 0$ theoretically signifies the stability of the interface, that is, no growth of the most unstable mode in this situation.

It turns out that the expression of \bar{k}_{max} for the PAA complex fluid is rather similar to its Newtonian counterpart. Similar to the Newtonian scenario, one noticeable result from Eq. (5) is that \bar{k}_{max} primarily varies with the interfacial velocity U_0 , which is increased with Q and (slightly) decreased with increasing $|\alpha|$ for a fixed h_f , the taper's thickness at the edge (see Fig. 2a). In addition, a converging gap gradient ($\alpha < 0$) helps reduce the value of \bar{k}_{max} , while an important difference in viscosity, via the local term of $\mu_2 - \mu_1$, has a destabilizing effect on the interface, enlarging the values of \bar{k}_{max} . A significant difference compared to the Newtonian case is that the viscosity terms now encompass the effect of complex fluids' yield-stress τ_c and other rheological parameters through k and n .

Using the wavenumber of maximum growth \bar{k}_{max} (Eq. 5) and the dimensionless dispersion relation (Eq. 4), we obtain the growth rate at the most unstable mode, $\bar{\sigma}(\bar{k}_{max})$. To compare with our theoretical prediction, we plotted in Fig. 3a the values of $\bar{\sigma}(\bar{k}_{max})$ using Eq. (4), with the values of viscosity (μ_1 and μ_2) and the velocity, location, and gap-thickness at propagating fluid-fluid interface (U_0 , r_0 and h_0) analyzed from the experiments. From Fig. 3a, we can observe a transition from stable (filled symbols) to unstable (open symbols) interfaces when $\bar{\sigma}(\bar{k}_{max}) < 7.5$ from the experimental data, slightly deviating from the theoretical value of $\bar{\sigma} < 0$ for a stable interface with a decay growth rate. In other words, the experimental values show a bound growth rate, i.e., a limited growth rate for the instability, while the experimental interface is still stable in reality. Figure 3b–d are the overlays of representative experimental snapshots, revealing the evolution of the interface profiles of stable (filled blue triangle) and unstable displacement (open blue triangle) for (S_b) while unstable interface (open orange diamond) for (S_a).

The deviation between our experimental results and theoretical prediction of the stable versus unstable displacement may be due to the few assumptions we made. For example, the impact of the gravity and the elastic properties have been ignored. Moreover, whenever $|\alpha|$ is getting bigger, the assumptions of small ratio of gap

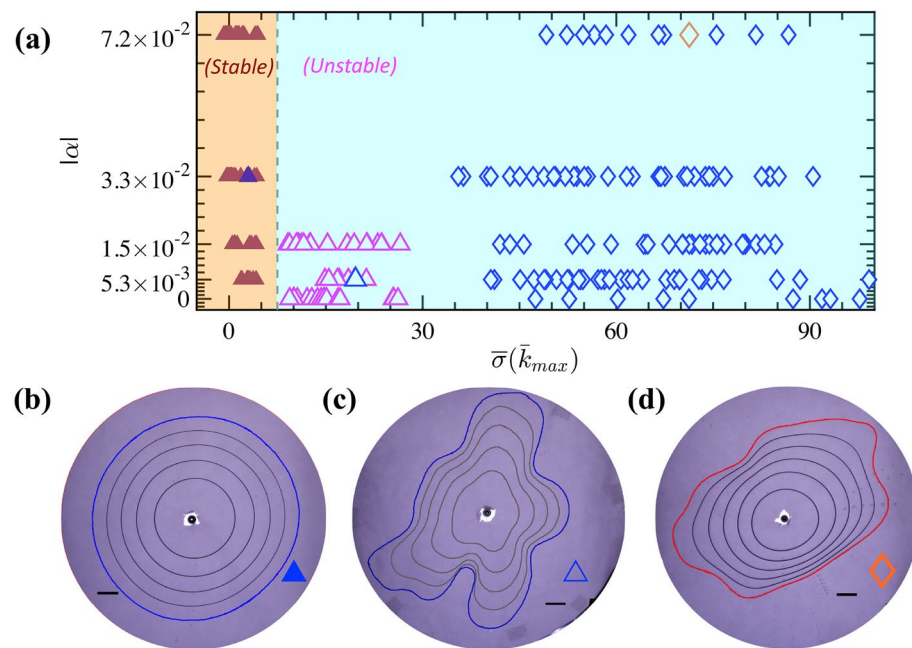


Figure 3. Comparison between experimental and theoretical results: **(a)** The growth rate of the perturbation at the most unstable mode of k_{max} , $\bar{\sigma}(\bar{k}_{max})$ using Eqs. (4) and (5) for different experiments performed with various gap-gradient, $|\alpha|$. The experiments with the more viscous solution (S_a) always show unstable wavy interface (\diamond). In contrast, for the less viscous complex fluid (S_b), stable displacement (\blacktriangle) and unstable interface (\triangle) are observed with nearly-zero and relatively-large growth rate $\bar{\sigma}$, respectively. Theoretically, stable interfaces occur with a negative growth rate, i.e., when $\bar{\sigma} < 0$. Consistently, our experiments show stable displacements (filled symbols) when $\bar{\sigma} < 7.5$. **(b)–(d)** are the overlays of experimental snapshots, revealing the evolution of the interface profiles for the three big symbols (\blacktriangle , \triangle , \diamond) in (a), respectively. The time steps are $\delta t = 22$ s, 0.6 s, and 1 s in (b), (c) and (d), respectively. Each scale-bar represents a length scale of 20 mm.

change ($\frac{\alpha(r-r_0)}{h_0} \ll 1$) as well as the characteristic length scale over which the depths varies being much larger than that of the perturbation scale ($\frac{kh_0}{\alpha r_0} \gg 1$) may not be applicable. Last but not the least, we neglected the yield stress compared to the viscous stress by assuming small $Bn \ll 1$. These assumptions likely contribute to the drifting of the critical growth rate at the most unstable mode from 0 (theoretically) to 7.5 (observed with our experimental conditions).

Conclusions

In summary, we have demonstrated a powerful way of stabilizing the primary viscous fingering instability for complex yield-stress, power-law fluids using a tapered narrow cell experimentally and theoretically for the first time. Experimentally, using a radially converging taper, we can hinder complex fingering patterns, e.g., eliminating side-fingers for the more-viscous (S_a) of $M_c \approx 10^4 - 10^7$ and suppressing wavy interfaces completely for the less-viscous complex fluid (S_b) of $M_c \approx 10^3 - 10^5$. With a linear stability analysis using the simplified, effective Darcy's law, we derive the dispersion relation and establish a convenient stability criterion corresponding to the perturbation's growth rate of the most unstable mode. In addition to the viscosity contrast ($\lambda = \mu_1/\mu_2$), gap gradient (α), θ_c and Capillary number (Ca) for the simple Newtonian fluids, several vital parameters affect the complex fluids' viscous fingering stability criterion, namely the fluid's rheological characteristics, such as κ , τ_c , n , and γ , as well as the interface position, gap thickness, and velocity (r_0 , h_0 and U_0 , respectively). Firstly, these parameters affects the value of the wavenumber of maximum growth k_{max} and the dispersion relation via the complex expression of the local viscosity for yield-stress fluids. Secondly, compared to the Newtonian dispersion relation, an additional (positive) term—depending on the yield-stress and power-law index of the fluids—appears in Eq. (4) for a converging taper, thereby destabilizing the interface and promoting fingering pattern for the complex fluids. This theoretical stability criterion through $\bar{\sigma}(k_{max})$, despite the assumption of small $Bn \ll 1$, shows fair agreement with the experimental results using two low yield-stress fluids of distinct mobility ratios. These results, particularly the complex dispersion relation (Eq. 4) and $\bar{\sigma}(k_{max})$, provide quantitative insights into the designs and strategies for controlling viscous fingering and interfacial profiles during complex fluids' displacement in microfluidics, narrow cells, packed beads, and porous media.

Methods

Sample preparation

The two aqueous solutions of PAA (SigmaAldrich, molecular weight: $M_w \approx 1,250,000$) are prepared to produce different viscosity contrasts. Both solutions have the same polymer concentration, by slowly adding the polymer powder in water and subsequently stirring the mixture at high speed for 1 hr. The mixture generates an acid solution that can be neutralized using a basic solution. The two PAA solutions: (S_a) and (S_b) are prepared with and without NaOH (S_b), respectively, by stirring them for another 10 hours at medium speed. Finally, after the agitation, the solution is allowed to rest for a day before performing rheological measurements.

Rheological measurements

We further perform oscillation amplitude sweep tests at constant frequency ($\hat{\omega} = 1$ rad/s) to validate negligible elasticity of the complex fluids. Shown in Fig. 4 below are the results of the loss factor, i.e., the ratio of the loss modulus (G'') to the storage modulus (G'). The former G'' represents the viscous properties of the complex fluids, while the latter G' fluid elasticity with respect to the shear stress, τ . The fluid's viscous behavior prevails when the loss factor (G''/G') is greater than unity, whereas elastic for $G''/G' < 1$. The vertical dashed lines represents the yield-stress values for the fluids (S_a) and (S_b). We only focus on the (color shaded) regime whereby fluids are flowing, i.e. $\tau > \tau_c$, when $G''/G' \gtrsim 1$, meaning the viscous component prevails. Hence, we can neglect the elastic effects of the fluids in the theoretical analysis.

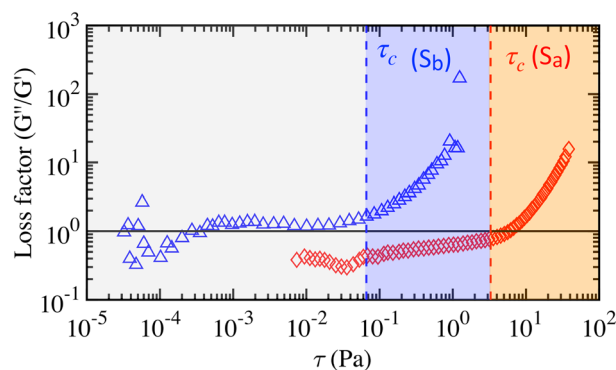


Figure 4. The data of loss factor, the ratio of the loss modulus (G'') to the storage modulus (G'), varying with the shear stress, τ , obtained during oscillation amplitude sweep test at constant frequency ($\hat{\omega} = 1$ rad/s). The vertical dashed lines represent the yield-stress (τ_c) values of the two fluids.

Data availability

Authors can confirm that all relevant data are included in the paper and/or its supplementary information files.

Received: 14 March 2023; Accepted: 16 January 2024

Published online: 29 January 2024

References

- Paterson, L. Radial fingering in a Hele Shaw cell. *J. Fluid Mech.* **113**, 513 (1981).
- Paterson, L. Fingering with miscible fluids in a Hele Shaw cell. *Phys. Fluids* **28**, 26 (1985).
- Saffman, P. G. Viscous fingering in Hele–Shaw cells. *J. Fluid Mech.* **173**, 73 (1986).
- Homsy, G. M. Viscous fingering in porous media. *Annu. Rev. Fluid Mech.* **19**, 271 (1987).
- Chen, J. D. Radial viscous fingering patterns in Hele–Shaw cells. *Exp. Fluids* **5**, 363 (1987).
- Dias, E. O. & Miranda, J. A. Control of centrifugally driven fingering in a tapered Hele–Shaw cell. *Phys. Rev. E* **87**, 053014 (2013).
- Chevalier, C., Ben Amar, M., Bonn, D. & Lindner, A. Inertial effects on Saffman–Taylor viscous fingering. *J. Fluid Mech.* **552**, 83 (2006).
- Rocha, F. M. & Miranda, J. A. Manipulation of the Saffman–Taylor instability: A curvature-dependent surface tension approach. *Phys. Rev. E* **87**, 013017 (2013).
- Park, S. S. & Durian, D. J. Viscous and elastic fingering instabilities in foam. *Phys. Rev. Lett.* **72**, 3347 (1994).
- Coussot, P. Saffman–Taylor instability in yield-stress fluids. *J. Fluid Mech.* **380**, 363 (1999).
- Fernandez, E. J., Norton, T. T., Jung, W. C. & Tsavalas, J. G. A column design for reducing viscous fingering in size exclusion chromatography. *Biotechnol. Prog.* **12**, 480 (1996).
- Pitts, E. & Greiller, J. The flow of thin liquid films between rollers. *J. Fluid Mech.* **11**, 33 (1961).
- Grillet, A. M., Lee, A. G. & Shaqfeh, E. S. Observations of ribbing instabilities in elastic fluid flows with gravity stabilization. *J. Fluid Mech.* **399**, 49 (1999).
- Green, D. W. & Willhite, G. P. *Enhanced Oil Recovery* 2nd edn. (SPE International Textbook, 2018).
- Cardoso, S. S. & Woods, A. W. The formation of drops through viscous instability. *J. Fluid Mech.* **289**, 351 (1995).
- Dias, E. O., Alvarez-Lacalle, E., Carvalho, M. S. & Miranda, J. A. Minimization of viscous fluid fingering: A variational scheme for optimal flow rates. *Phys. Rev. Lett.* **109**, 144502 (2012).
- Zheng, Z., Kim, H. & Stone, H. A. Controlling viscous fingering using time-dependent strategies. *Phys. Rev. Lett.* **115**, 174501. <https://doi.org/10.1103/PhysRevLett.115.174501> (2015).
- Pihler-Puzović, D., Illien, P., Heil, M. & Juel, A. Suppression of complex finger-like patterns at the interface between air and a viscous fluid by elastic membranes. *Phys. Rev. Lett.* **108**, 074502 (2012).
- Pihler-Puzović, D., Périllat, R., Russell, M., Juel, A. & Heil, M. Modelling the suppression of viscous fingering in elastic-walled Hele–Shaw cells. *J. Fluid Mech.* **731**, 162 (2013).
- Al-Housseiny, T. T., Christov, I. C. & Stone, H. A. Two-phase fluid displacement and interfacial instabilities under elastic membranes. *Phys. Rev. Lett.* **111**, 034502 (2013).
- Al-Housseiny, T. T., Tsai, P. A. & Stone, H. A. Control of interfacial instabilities using flow geometry. *Nat. Phys.* **8**, 747 (2012).
- Al-Housseiny, T. T. & Stone, H. A. Controlling viscous fingering in tapered Hele–Shaw cells. *Phys. Fluids* **25**, 092102 (2013).
- Bongrand, G. & Tsai, P. A. Manipulation of viscous fingering in a radially tapered cell geometry. *Phys. Rev. E* **97**, 061101 (2018).
- Mirzadeh, M. & Bazant, M. Z. Electrokinetic control of viscous fingering. *Phys. Rev. Lett.* **119**, 174501 (2017).
- Herschel, W. H. & Bulkley, R. Konsistenzmessungen von gummi-benzollösungen. *Kolloid Z.* **39**, 291 (1926).
- Maleki-Jirsaraei, N., Lindner, A., Rouhani, S. & Bonn, D. Saffman–Taylor instability in yield stress fluids. *J. Phys. Condens. Matter* **17**, 1219 (2005).
- Eslami, A. & Taghavi, S. M. Viscous fingering regimes in elasto-visco-plastic fluids. *J. Non-Newton. Fluid Mech.* **243**, 79 (2017).
- Eslami, A. & Taghavi, S. M. Viscous fingering of yield stress fluids: The effects of wettability. *J. Non-Newton. Fluid Mech.* **264**, 25 (2019).
- Eslami, A., Basak, R. & Taghavi, S. M. Multiphase viscoplastic flows in a nonuniform Hele–Shaw cell: A fluidic device to control interfacial patterns. *Ind. Eng. Chem. Res.* **59**, 4119 (2020).
- Kondic, L., Palfy-Muhoray, P. & Shelley, M. J. Models of non-Newtonian Hele–Shaw flow. *Phys. Rev. E* **54**, R4536. <https://doi.org/10.1103/PhysRevE.54.R4536> (1996).
- Talon, L. & Bauer, D. On the determination of a generalized Darcy equation for yield-stress fluid in porous media using a lattice-Boltzmann TRT scheme. *Eur. Phys. J. E Soft Matter* **36**, 139. <https://doi.org/10.1140/epje/i2013-13139-3> (2013).
- Lindner, A., Bonn, D. & Meunier, J. Viscous fingering in a shear-thinning fluid. *Phys. Fluids* **12**, 256 (2000).

Acknowledgements

A.P. and P.A.T. thankfully acknowledge the funding support from the Natural Sciences and Engineering Research Council of Canada (NSERC) Discovery grant (RGPIN-2020-05511) and from the Alberta Innovates (AI Advance 222302054). P.A.T. holds a Canada Research Chair in Fluids and Interfaces (CRC TIER2 233147). This research was undertaken, in part, thanks to funding from the Canada Research Chairs (CRC) Program.

Author contributions

A.P.: Methodology, Investigation, Validation, Formal analysis, Visualization, Writing—Original draft preparation; P.A.T.: Conceptualization, Methodology, Investigation, Formal analysis, Validation, Visualization, Supervision, Funding acquisition, Writing—Review & Editing.

Competing interests

The authors declare no competing interests.

Additional information

Supplementary Information The online version contains supplementary material available at <https://doi.org/10.1038/s41598-024-52218-w>.

Correspondence and requests for materials should be addressed to P.A.T.

Reprints and permissions information is available at www.nature.com/reprints.

Publisher's note Springer Nature remains neutral with regard to jurisdictional claims in published maps and institutional affiliations.



Open Access This article is licensed under a Creative Commons Attribution 4.0 International License, which permits use, sharing, adaptation, distribution and reproduction in any medium or format, as long as you give appropriate credit to the original author(s) and the source, provide a link to the Creative Commons licence, and indicate if changes were made. The images or other third party material in this article are included in the article's Creative Commons licence, unless indicated otherwise in a credit line to the material. If material is not included in the article's Creative Commons licence and your intended use is not permitted by statutory regulation or exceeds the permitted use, you will need to obtain permission directly from the copyright holder. To view a copy of this licence, visit <http://creativecommons.org/licenses/by/4.0/>.

© The Author(s) 2024